SAND2022-5216C

ILASS-Americas 32nd Annual Conference on Liquid Atomization and Spray Systems, May 22-25, 2022

Detailed evaporation modelling for gasoline direct injection: iso-octane vs. E30

M. Arienti*, and E.A. Wenzel
Sandia National Laboratories
Livermore, CA 94550, USA

Abstract

Gasoline direct injection (GDI) promises better fuel economy and superior performance in internal combustion engines when compared to conventional gasoline port fuel injection. In this presentation, a sharp-interface method for the multiphase Navier-Stokes equations (the CLSVOF computer code developed by Prof. M. Sussman), coupled to a new mass- and energy-conserving numerical method for surface evaporation, is applied to calculate vapor concentration close to the injector. The injector geometry of interest is the eight-hole counterbored GDI injector (spray G in the ECN denomination) both with fully unseated and partially closed pintle. Experimental data about vapor concentration from the recessed region inside the counterbores are difficult to obtain due to limited optical access, while conventional computational fluid dynamics methodologies are unable to accurately account for phase change at the liquid surface. In the framework of the proposed computational approach, GDI sensitivity to fuel properties is assessed by considering neat iso-octane and the homogenous mixture of 30% ethanol and 70% iso-octane in volume (E30). Compared to a previous case study where evaporation was not included, the near-orifice fuel temperature increase due to heat transfer from the hot gas is reduced by the cooling effect of evaporation, as expected. We find that during the closing transient, when gas recirculation in the counterbore decreases because of the diminishing entrainment by the jet, evaporative cooling becomes stronger, but only for E30.

*Corresponding Author: marient@sandia.gov

Introduction

The work is aimed at quantitatively characterizing the changes in operation of a multi-hole Gasoline Direct Injection (GDI) atomizer due to differences in fuel volatility. Blends of biofuel and hydrocarbon components into gasolines are experiencing renewed interest because of the potential for higher latent heat of vaporization to increase fuel knock resistance in direct-injection (DI) engines. The GDI multi-hole configuration is relevant because of its ability to directly target fuel to the spark plug for stratified operation and to different areas around the cylinder for robust mixture formation. The need to better control the mixture properties is further emphasized by the trend towards using sustainable renewable fuels in increasing proportions with gasoline.

With increasing interest in understanding the effects on NOx and soot formation by blending gasoline with bio-components that alter the fuel specific thermo-physical and chemical properties, recent studies have focused on the addition of ethanol. One of the advantages of ethanol addition is charge cooling, which results in lower charge temperature at the start of combustion and reduces the rate of autoignition kinetics [1]. High-speed imaging and droplet sizing in an optical direct injection spark ignition engine have shown that spray and combustion characteristics differ for E85 and gasoline [2]. For GDIs at high ambient temperature conditions (673 K and 1.5 MPa in their experiments), Zigan et al. concluded that droplet size and momentum are mainly controlled by evaporation [3]. In general, for low and moderate ambient temperature and pressure, high-boiling point components show a strong influence on the spray droplet size distribution, whereas the evaporation cooling effect dominates at elevated temperature and pressure; fuel mixtures with larger heat of vaporization show larger droplet sizes even if these fuels have a lower boiling point [4]. Differences in the atomization process can be substantial. Near-orifice fuel density was measured by tomographic x-ray radiography for neat iso-octane and a blend of 80% iso-octane with either 20% butanol or 20% ethanol at elevated injection temperatures into a sub-atmospheric environment [5]. Combined with USAXS measurements for the Sauter mean diameter, these techniques indicated a different atomization process for E20, possibly caused by flash boiling, that correlates with the lower boiling temperature of ethanol.

From a modeling point of view, while experiments that describe single droplet evaporation have long been incorporated in spray models, phase transition processes of dense sprays under high pressure and turbulence conditions can be expected to be more complex. Thus, the approximation limits concerning the description of a fuel jet as a collection of isolated droplets (Lagrangian-Eulerian models [6] [7]) requires further assessment. In this context, it is worth noting that diffuse-interface Eulerian methods with volume of fluid (VOF) advection, but no surface reconstruction, are often used in near-nozzle injection simulation [8],[9]; while potentially effective in describing phase change in the liquid bulk (cavitation and flash boiling), these methods lack a precisely identifiable liquid surface and therefore cannot correctly account for evaporation. The effect of fuel properties was examined by Yue and Som [10] using VOF piecewise-linear interface reconstruction without finding noticeable differences between the injection of iso-octane and of E30. That study, however, as well as a following eight-holes simulation by the authors [11], did not include evaporation effects.

Prior work has demonstrated the framework of Jemison et al. [12] to accurately model compressible, weakly cavitating sprays in realistic injector geometries [11]. A new numerical method has since been developed to incorporate evaporation and boiling as described in [13] and in an upcoming paper [14]; this capability allows for variable density in the liquid and gas phases, enforces numerical consistency in the rates of mass and energy transport, and conserves mass, momentum, and energy.

In the following, the sensitivity of direct fuel injection to the addition of ethanol is examined in a 30-70 mixture by volume with iso-octane used as gasoline surrogate. First, the thermo-physical properties of E30 that are most relevant to evaporation are summarized and compared to those of iso-octane and ethanol, showing that they cannot be obtained by linear combination of the components. The Peclet number of the mixture is also introduced, as an index of the tendency of the mixture toward de-mixing of the light and heavy component that is specific to the injection conditions. The description of the numerical method is briefly summarized, given its complexity and the availability of sufficient references; similarly, the reduction of the x-radiography scanning data of the injector's surfaces to computational boundaries is not discussed in depth. The focus of this study is the simulation of the two situations of fully open and partially closed injector in the presence of evaporation; the main result is the temperature of the fuel jets as they pass through the counterbores into the near-field volume of gas. Integral values of mass rate of evaporation and exposed liquid surface are then used to estimate the regression rate of the surface and the average Peclet number

that is found at the high pressure and temperature conditions of the injection.

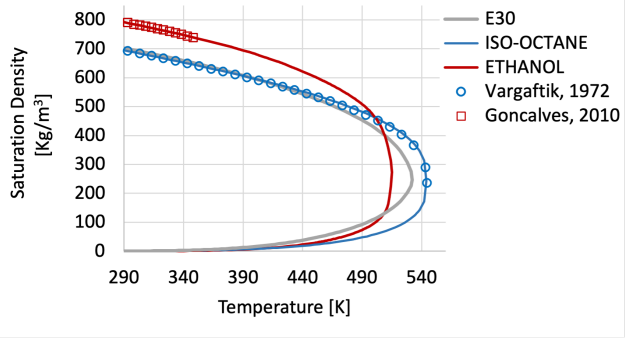

Figure 1. Saturation liquid and vapor densities from REFPROP [15] compared to experimental data for the neat components [16] [17].

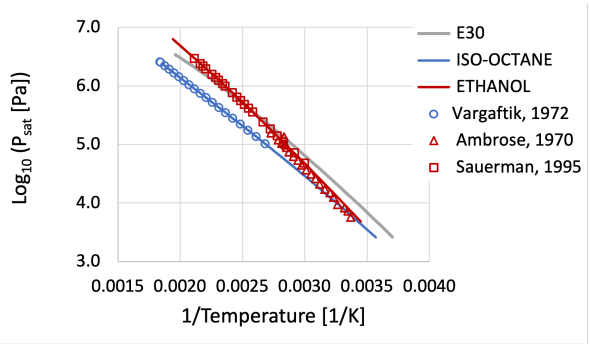

Figure 2. Saturation pressure from REFPROP [15] compared to experimental data for the neat components [18] [19].

Thermo-physical properties of E30

Because alcohol is a polar substance and iso-octane is non-polar, gasoline/ethanol blends do not behave like an ideal mixture [23] [24]. In a modeling approach that aims to detect the dependence of direct fuel injection on the fuel mixture properties, it is therefore necessary to establish whether the concentration of the most volatile species [3] needs to be tracked as in a distillation process, or if the the process can be considered one of co-evaporation. This assessment depends on the experimental conditions as well as on the fuel mixture, and it is typically carried out assuming a spherical evaporating droplet [25]. These considerations can be extended to include the complex morphology of an atomizing spray and its surrounding gas flow as follows.

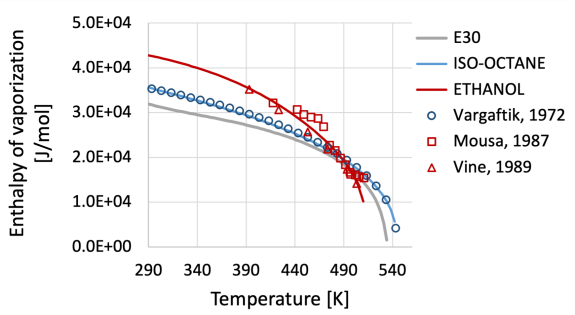

Figure 3. Enthalpy of vapor formation from REFPROP [15] compared to experimental data for the neat components [17] [20] [21].

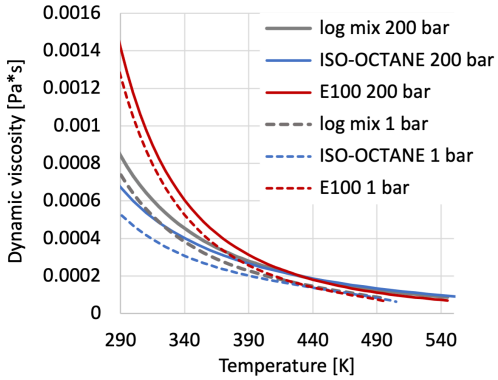

Figure 4. Dynamic viscosity at 1 and 200 bar (dashed and continuous lines, respectively.) The curves for ethanol and iso-octane are calculated from REFPROP [15], whereas the E30 curves are obtained using the simplified Grunberg–Nissan model [22].

The Peclet number for mass diffusion is

$$\mathrm{Pe}_l = \frac{K_s}{D_l} \tag{1}$$

where K_s is the liquid surface regression rate and D_l the liquid mass diffusion, in our case of ethanol into iso-octane. For a spherical droplet of radius r_s, the instantaneous regression rate is [25]

$$K_s = -\frac{1}{2}\frac{d}{dt}r_s^2. \tag{2}$$

This expression can be generalized in the form

$$K_s = h_s v_s, \tag{3}$$

taking v_s to be the instantaneous regression rate and h_s a characteristic depth of the liquid in the evaporation interval; for a spherical droplet, $h_s = r_s$.

The evaporation process is dominated by distillation if $\mathrm{Pe}_l \ll 1$, whereas it is liquid diffusion-limited if $\mathrm{Pe}_l \gg 1$. In the latter case, co-evaporation of the components of the fuel mixture is assumed. This will also be our hypothesis for E30, as it is often done for fuel mixtures under high pressure and high temperature conditions [25]; we will check if this assumption is correct in the analysis of the results.

In this work, the properties of E30 (as well as of iso-octane) are calculated by the REFPROP library [15], either by directly using the subroutines accompanying the NIST program, or by custom correlations derived from REFPROP-generated diagrams. The results concerning phase change are shown for the liquid/vapor saturation densities in Figure 1, for the saturation pressure in Figure 2, and for the enthalpy of vaporization in Figure 3. For the dynamic viscosity of the binary mixture E30, the simplified Grunberg-Nissan model $\ln \mu = x_1 \ln \mu_1 + x_2 \ln \mu_2$ [22] is used, where x is the mole fraction and subscripts 1 and 2 denote the mixture components. The plot in Figure 4 shows that, in the fixed composition of interest here, μ_{E30} is closer to μ_{iso} at lower temperatures and closer to μ_{E100} at higher temperatures. Finally, surface tension is fixed at 20 mN/m for iso-octane and at 22 mN/m for E30.

Numerical method

The multi-phase compressible Navier-Stokes equations are solved with the directionally-split, Cell-Integrated Semi-Lagrangian advection algorithm of Jemison et al. [12]. The solution is advanced in time by a semi-implicit pressure update scheme that asymptotically preserves the standard incompressible pressure projection in the limit of infinite sound speed. Following the Moment of Fluid Method [26], the piecewise-linear reconstruction of the gas-liquid interface is obtained from the location of the phase centroid of the material in the computational cell and from the local values of level set (LS) and volume of fluid (VOF). The interface is reconstructed at every iteration with at least first-order accuracy with respect to slope reconstruction [12].

As in [27], the walls of the injector are represented by an embedded boundary where the magnitude of the signed distance function is the distance from the cell center to the solid and the sign is negative inside the solid. The evaluation of the boundary normal from this level set function avoids staircase-like artifacts in the solution. The procedures for populating center and face values in the solid ghost region are described in [28]. When applied to moving solid surfaces, such as during the unseating of the injector's pintle, the embedded boundary can cross the computational Cartesian cells; contact and separation of wall surfaces are handled as logical operations on the level set function. The pintle lift trajectory is reported in [5].

Computational setup

The experimental conditions set for Spray G by the ECN (G1 conditions [29]) consist of a vessel filled with nitrogen gas at temperature 573 K and density 3.5 kg/m^3 (corresponding to 6×10^5 Pa). In the baseline setting for iso-octane, the fuel is injected at 2×10^7 Pa and 363 K; the same conditions are used for E30. The injector is assumed to maintain a constant temperature of 343 K. Pressure and temperature at the inlet and outlet are kept constant during the simulation; the instantaneous flow rate is therefore the result of resistance to the passage of the liquid through the injector's geometry.

Nominally, the eight-hole Bosch injector spray G has identical inner orifice diameter of 0.165 mm, inner counterbore diameter of 0.388 mm and drill angle of 37°. The actual spray G nozzle geometry, measured by x-ray computed tomography (CT) imaging to a resolution as small as 1.17 μm [30], shows deviations with respect to the nominal geometry, such as hole-to-hole variations in orifice diameters and inlet radii of curvature. For use in the simulations, the scanned geometry surfaces of spray G #28 are represented by two distinct triangular tessellations, one for the outer injector and one for the pintle. At start time, the surfaces are reconstructed in CLSVOF as separate level set functions; during the simulation the pintle is moved according to the prescribed trajectory to realize the opening and closing of the fuel passages. The injection command duration is 0.680 ms; the maximum pintle displacement at 51 μm is achieved between 0.1 and 0.6 ms after start of injection.

The computational domain is a $6 \times 6 \times 6$ mm cube centered at the injector's tip; Figure 5 displays a cross-section of the injector from the reconstructed tomographic images where the dashed lines indicate the boundaries of the computational domain. According to the orientation convention established by the ECN and shown in Figure 6(a), the positive Z-axis corresponds to the injector axis and the origin of the coordinate system is at the nozzle tip. The base block is a 256^3 cell Cartesian box, which is further subdivided in 16^3 blocks. Two levels of refinement are added in the simulation to reach the grid resolution $\Delta \mathrm{x}_{\mathrm{min}} = 5.86$ μm at the liquid interface. As noted in [11] for these same injection conditions, this grid density is not sufficient to capture the for-

mation of very small droplets, but it is deemed sufficient to capture the main features of the jets and vapor plumes for the duration of the injection interval. While varying because of the application of adaptive mesh refinement, a reference cell count is of approximately of 450 million. Calculations were carried out at Sandia National Laboratories on the HPC Production Linux Clusters: Sky Bridge and Chama (Cray 2.6 GHz Intel Sandy Bridge 16 cores/node, InfiniBand interconnect), and Ghost (2.1 GHz Intel Broadwell 36 cores/node, Omni-Path interconnect).

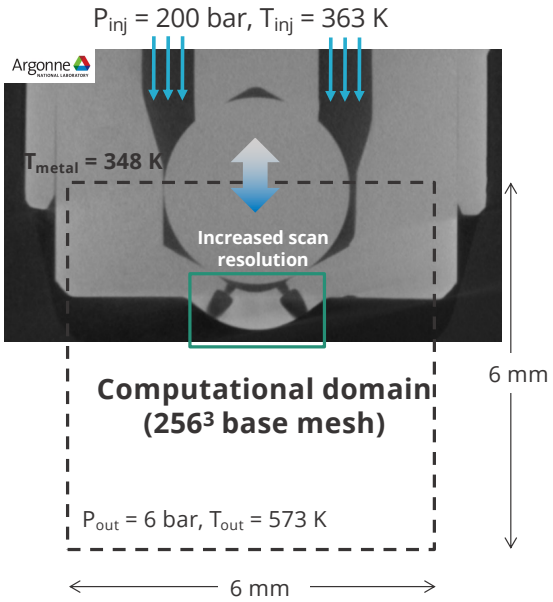

Figure 5. Cross-section of the injector from reconstructed tomography with domain boundary conditions.

Results

We first examine the spray features in the presence of evaporation at fully open conditions. Spray G simulation results at the same conditions and for the same computational setup have been already examined by the authors [11], but in the artificial situation of no evaporation. Instantaneous snapshots of the eight jets from spray G are shown for iso-octane and E30 in Figure 9 and 10. The liquid surface is rendered as the zero-value level set function and colored by temperature; vapor concentration is represented by the superposition of iso-surfaces at values 0.1, 0.25 and 0.50 of mass fraction. For ease of visualization, the injector's surface is not plotted; note that the extent of the internal flow can be tracked by the lower temperature values of the liquid surface

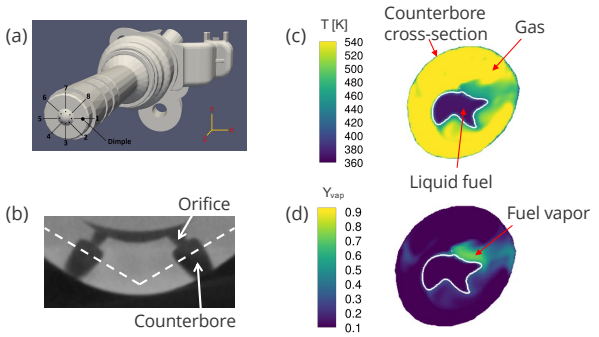

Figure 6. (a) Spray G drawing with ECN orientation. (b) Intersection of the slicing conical surface (dashed line) – used for visualization purposes in Figures 11 and 12 – with the side cross-section of the injector's tomographic reconstruction (courtesy of ANL). (c) Closeup of the counterbore interior showing the separation of liquid from gas. (d) Same closeup showing the instantaneous distribution of vapor mass fraction.

there. The spray angle appears larger for E30 than for iso-octane – a result consistent with the spray angle measurements for E85 and iso-octane for 1.0 bar gas pressure that are reported in [2]. In comparing the two snapshots, one can also see that the surface temperature of liquid iso-octane is a few degrees higher than the temperature of E30, reaching or surpassing 400 K at certain locations. Consistently, the vapor concentration of E30 is larger and vapor completely envelops the liquid jets in Figure 10. We conclude that evaporation cooling keeps the surface temperature of liquid E30 closer to the value at injection.

A closer look at the liquid jets reveals that outside of the injector they tend to develop in narrow sheets rather than maintain a circular shape. Figure 7 shows their superposition in time on the $Z = 1$ mm plane for iso-octane; most of the contour shapes appear elongated and curly (these cross-sections bear some similarity with the ones reported by [10]), but, due to the unsteadiness of the flow, their superposition aggregates in a roughly circular form. This picture can be compared with the top-left insert of Figure 7, displaying the time-averaged density scan from x-radiography at similar conditions and at the same distance from the injector's tip (see also [5], [11]). It is noted that the x-radiography scan was averaged for 200 μs, whereas the simulation was averaged with 20 snapshots on a much smaller interval of 25 μs.

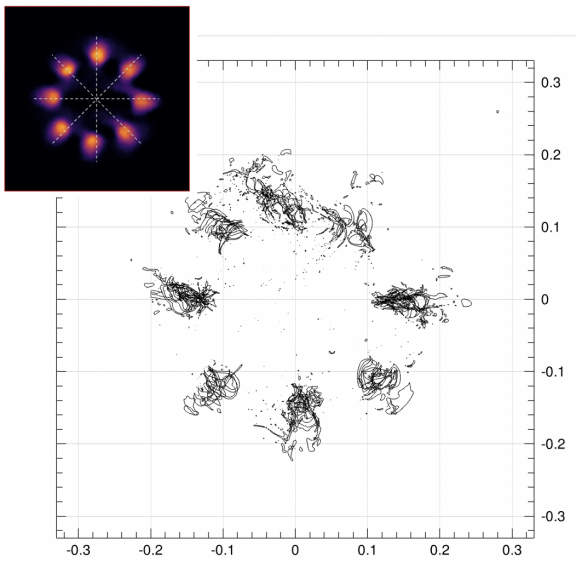

Figure 7. Fully open injector, iso-octane: superposition of liquid jet cross-sections on the $Z = 1$ mm plane. The top-left insert displays the time-averaged cross-sectional density scan from x-radiography by ANL [5].

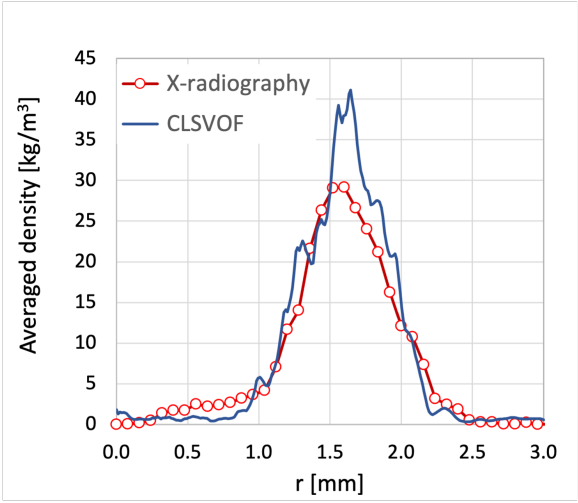

Figure 8. Fully open injector, iso-octane: comparison of the averaged density across the eight jets.

A more direct comparison with the radiography data is shown in Figure 8, where density profiles as function of radial distance are obtained as the average of the plume densities along four planes cut through the geometrical axis of the injector and rotated by increments of 45° (the traces of these planes are shown as dashed lines in the top left insert of Figure 7). The same procedure is applied to the simulation results for iso-octane, showing that the average jet direction is well captured. The larger peak value of the simulation in Figure 8 can be explained in terms of the jets being more closely aligned with the sampling planes and less disperse than in the experiment; given the small sampling interval, there is also a large variability from snapshot to snapshot that results in a strong dependence on the alignment of the sampling planes with the center of the jets.

Considering now the evaluation of the Peclet number for the liquid jets, a reference velocity regression can be established from the values of exposed liquid surface and of evaporating mass extracted from the simulation: for iso-octane $v_r \approx 0.6\,\mathrm{cm/s}$, and for E30 $v_r \approx 0.7\,\mathrm{cm/s}$. These are only integral values, whereas variations in surface temperature, flow field, and vapor concentration in the gas phase can make the local v_r much smaller or much larger. Since the peak in distribution of the Sauter Mean Diameter measured for iso-octane at the current injection conditions is approximatively $10\,\mu$m ([31] [5]), it is convenient to take $h_s = 5\,\mu$m as reference length; this value is also close to the product of the injection interval times v_r. The corresponding regression rate is therefore $K_s = 3.5 \times 10^{-4}\mathrm{cm}^2/\mathrm{s}$.

The value of diffusion coefficient for E30 into iso-octane is not directly available from published measurements, but the following estimate is obtained using the Wilke-Chang equation described by Reid [32]: $D_l = 10^{-4}$ cm^2/s. For comparison, the measured diffusion coefficient of benzene into ethanol is $D_l = 5.5 \times 10^{-5}$ cm^2/s at 373 K [33]. With estimates of K_s and D_l it is possible to calculate Pe = 3.5 from Eqn. 1; we therefore find that, at G1 conditions, evaporation is sufficiently fast, on average, to avoid considering the change in composition of the liquid phase, at least in very first approximation.

Evaporation accounts for a loss of liquid fuel mass between 0.4 to 0.7 g/s within the computational domain; this is a rather small percentage of the total injected mass flow (for iso-octane, $\dot{m} = 14\,\mathrm{g/s}$), but its effects at the injector become more evident toward the end of injection. To examine the flow inside the counterbores, it is convenient to cut the computational domain with a surface that is perpendicular to their axes. This surface is a cone, aligned with the nominal axis of symmetry of the injector, whose half angle is equal to the nominal angle of the orifices; its trace is shown in Figure 6(b) as a dashed line. Figures 11 and 12 are then a representation of the flow crossing the eight counterbores

holes on the surface of the cutting cone: the liquid surface is marked with a continuous white line, and temperature (top row) and mass fraction of vapor in the N_2-vapor mixture (bottom row) are plotted in the space between the liquid and the injector's wall. In Figure 11 snapshots for iso-octane and E30 are taken at fully open injector conditions, whereas in Figure 12 the two snapshots are taken as the injector's gap is at 20 μm.

The most remarkable difference in the two plots is the gas temperature distribution. As long as injector remains open, the entrainment of the high-velocity liquid jets is sufficient to create enough gas recirculation in the counterbores for the temperature there to be as high as the gas temperature outside of the injector. When the fuel passages become narrower and the jets begin to slow down, the gas remains in the counterbores longer and its temperature decreases because of evaporative cooling. This effect is much more pronounced in the case of E30.

Conclusions

In this study, we have highlighted a few aspects linked to evaporation in GDI of E30 compared to neat iso-octane. Thanks to a recently developed model for surface evaporation at a sharp interface, it is now possible to visualize and quantify the fuel mass evaporated in the dense spray region that forms near the injector. While the available grid resolution is not sufficient to capture the smallest droplets formed by primary atomization, the simulation results point to differences in exit fuel temperatures that should inform future GDI engineering simulations. Immediately after injection, the jets tend to flatten in narrow sheets that increase the fuel surface exposed to the hot gas; only with the superposition of several instantaneous snapshots of density distribution it is possible to visualize the more circular cross-sections observed in time-averaged images of the jets.

At the elevated chamber temperature and pressure of the G1 conditions, differences in viscosity between the two fuels cause a larger spray angle in E30 than in iso-octane, consistent with observations for fuel with higher ethanol content. Evaporation cooling emerges as a dominant effect that differentiates the two fuels during injection closing, when recirculation in the counterbores decreases because of the diminished gas entrainment by the jets; gas cooling is much more pronounced for E30.

On average, we also found that the evaporation rate of E30 is sufficiently faster than diffusion in the liquid phase to justify the use of a homogenous mixture model in the numerical approach, i.e., the Peclet liquid number is greater than one. This observation does not exclude areas on the liquid surface where the co-evaporation assumption might be more questionable. Work is in progress to statistically analyze the simulation results and provide further insight into the sensitivity of direct fuel injection to the thermo-physical properties of the fuel.

Acknwoledgments

This research was conducted as part of the Co-Optimization of Fuels and Engines (Co-Optima) project sponsored by the U.S. Department of Energy (DOE) Office of Energy Efficiency and Renewable Energy (EERE), Vehicle Technologies Office. Sandia National Laboratories is a multi-mission laboratory managed and operated by National Technology and Engineering Solutions for Sandia LLC, a wholly owned subsidiary of Honeywell International Inc., for the U.S. Department of Energy's National Nuclear Security Administration under contract DE-NA0003525.

References

[1] R.A. Stein, J.E. Anderson, and T.J. Wallington. *SAE International Journal of Engines*, 6(1):470–487, 2013.

[2] P.G. Aleiferis, J. Serras-Pereira, Z. Van Romunde, J. Caine, and M. Wirth. *Combustion and Flame*, 157(4):735–756, 2010.

[3] L. Zigan, I. Schmitz, A. Flügel, T. Knorsch, M. Wensing, and A. Leipertz. *Energy & fuels*, 24(8):4341–4350, 2010.

[4] T. Knorsch, M. Heldmann, L. Zigan, M. Wensing, and A. Leipertz. *Experiments in fluids*, 54(6):1–14, 2013.

[5] B.A. Sforzo, A. Tekawade, K. Matusik, A. Kastengren, J. Ilavsky, and C. Powell. *ILASS-Europe 2019, 29th Conference on Liquid Atomization and Spray Systems*, September 2019.

[6] A. Muddapur, J.V. Jose, S. Sahu, and T. Sundararajan. *Fuel*, 279:118057, 2020.

[7] Q. Jiao, Y. Ra, and R.D. Reitz. Modeling the influence of molecular interactions on the vaporization of multi-component fuel sprays. Technical report, SAE Technical Paper, 2011.

[8] E.T. Baldwin, R.O. Grover Jr, S.E. Parrish, D.J. Duke, K.E. Matusik, C.F. Powell, A.L. Kastengren, and D.P. Schmidt. *International Journal of Multiphase Flow*, 87:90–101, 2016.

[9] K. Saha, S. Som, M. Battistoni, Y. Li, E. Pomraning, and P.K. Senecal. *SAE International Journal of Engines*, 9(2):1230–1240, 2016.

[10] Z. Yue and S. Som. Fuel property effects on spray atomization process in gasoline direct injection. Technical report, SAE Technical Paper, 2020.

[11] M. Arienti, E.A. Wenzel, B.A. Sforzo, and C.F. Powell. *Proc. Combust. Inst.*, 2020.

[12] M. Jemison, M. Sussman, and M. Arienti. *J. Comput. Phys.*, 279:182–217, 2014.

[13] M. Arienti and E.A. Wenzel. *ILASS-Americas 2021, 31st Annual Conference on Liquid Atomization and Spray Systems*, May 2021.

[14] E.A. Wenzel and M. Arienti. *Submitted to J. Comput. Phys.*

[15] E.W. Lemmon, I.H. Bell, M.L. Huber, and M.O. McLinden. NIST Standard Reference Database 23: Reference Fluid Thermodynamic and Transport Properties-REFPROP, Version 10.0, National Institute of Standards and Technology, 2018.

[16] F.A.M.M. Gonçalves, A.R. Trindade, C.S.M.F. Costa, J.C.S. Bernardo, I. Johnson, I.M.A Fonseca, and A.G.M Ferreira. *The Journal of Chemical Thermodynamics*, 42(8):1039–1049, 2010.

[17] N.B. Vargaftik, L.P. Filippov, A.A. Tarzimanov, E.E. Totskii, and Y.A. Gorshkov. *Handbook of thermal conductivity of liquids and gases*. CRC press, 2020.

[18] D. Ambrose and C.H.S Sprake. *The Journal of Chemical Thermodynamics*, 2(5):631–645, 1970.

[19] P. Sauermann, K. Holzapfel, J. Oprzynski, F. Kohler, W. Poot, and T.W. de Loos. *Fluid phase equilibria*, 112(2):249–272, 1995.

[20] A.H.N. Mousa. *Journal of chemical engineering of Japan*, 20(6):635–637, 1987.

[21] M.D. Vine and C.J. Wormald. *The Journal of Chemical Thermodynamics*, 21(11):1151–1157, 1989.

[22] B.E. Poling, J.M. Prausnitz, J.P. O'connell, et al. *The properties of gases and liquids*, volume 5. Mcgraw-hill New York, 2001.

[23] B. Waluyo, I.N.G. Wardana, L. Yuliati, and M.N. Sasongko. *Fuel*, 215:178–186, 2018.

[24] P. Keller, T. Knorsch, M. Wensing, and C. Hasse. *International Journal of Heat and Mass Transfer*, 84:497–510, 2015.

[25] A. Makino and C.K. Law. *Combustion and flame*, 73(3):331–336, 1988.

[26] M. Jemison, E. Loch, M. Sussman, M. Shashkov, M. Arienti, M. Ohta, and Y. Wang. *Journal of Scientific Computing*, 54(2):454–491, 2013.

[27] M. Arienti and M. Sussman. *International Journal of Multiphase Flow*, 88:205–221, 2017.

[28] M. Arienti and M. Sussman. *International Journal of Multiphase Flow*, 59:1–14, 2014.

[29] https://ecn.sandia.gov/data/sandia-spray-g-data/.

[30] D.J. Duke, A.L. Kastengren, K.E. Matusik, A.B. Swantek, C.F. Powell, R. Payri, D. Vaquerizo, L. Itani, G. Bruneaux, R.O. Grover Jr, et al. *Experimental Thermal and Fluid Science*, 88:608–621, 2017.

[31] Engine combustion network, ecn4 proceedings 2014 available at https://ecn.sandia.gov/ecn-workshop/ecn4-workshop/.

[32] R.C. Reid, J.M. Prausnitz, and B.E. Poling. *The properties of gases and liquids*. McGraw Hill Book Co., New York, NY, 1987.

[33] T. Tominaga and S. Matsumoto. *Bulletin of the Chemical Society of Japan*, 63(2):533–537, 1990.

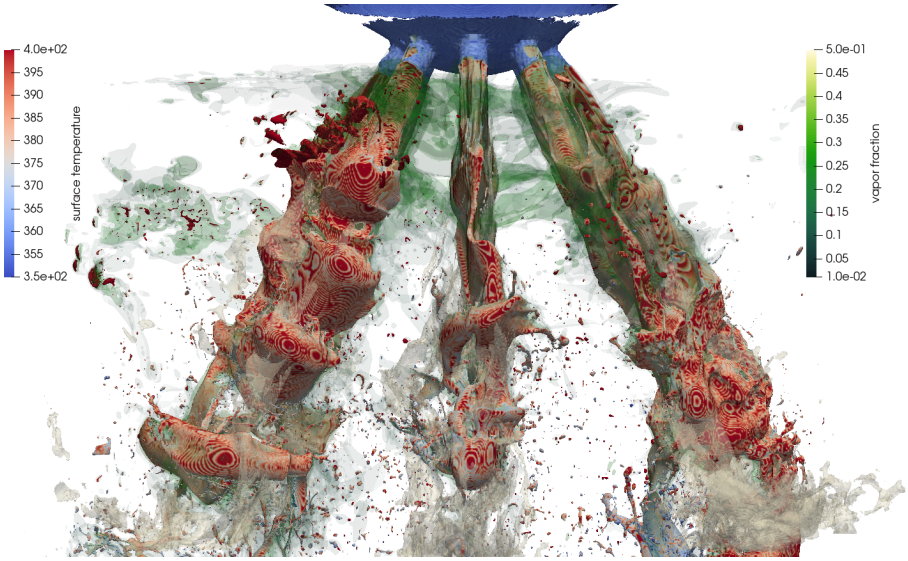

Figure 9. Fully open sprayG. Instantaneous snapshots of iso-octane spray jets and vapor concentration.

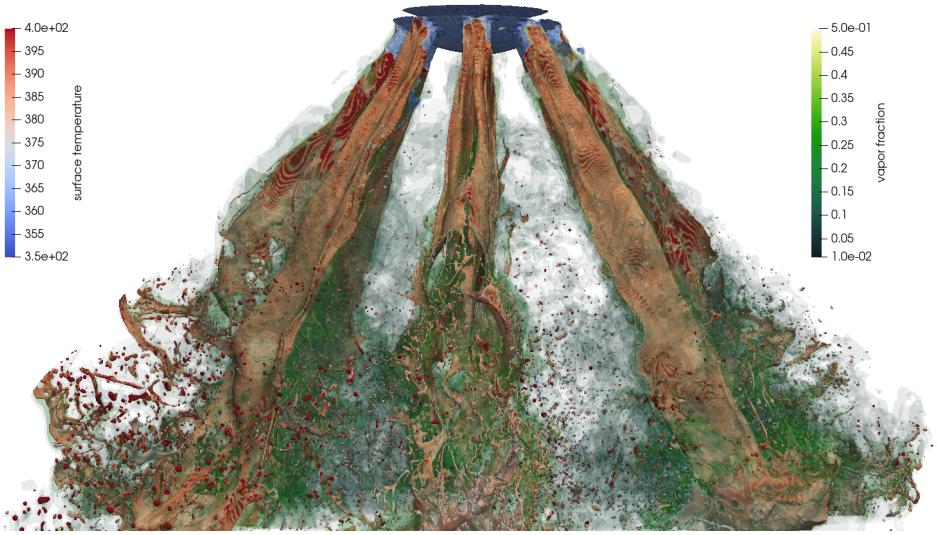

Figure 10. Fully open sprayG. Instantaneous snapshots of E30 spray jets and vapor concentration.

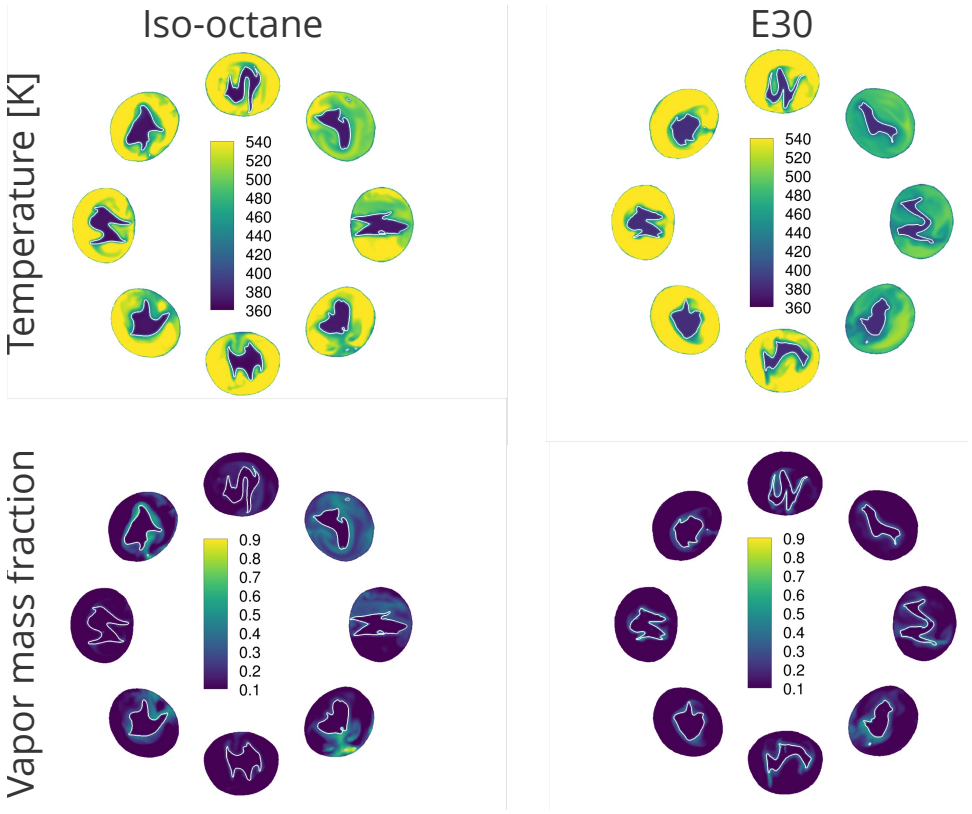

Figure 11. Flow passing through the counterbores at fully open conditions.

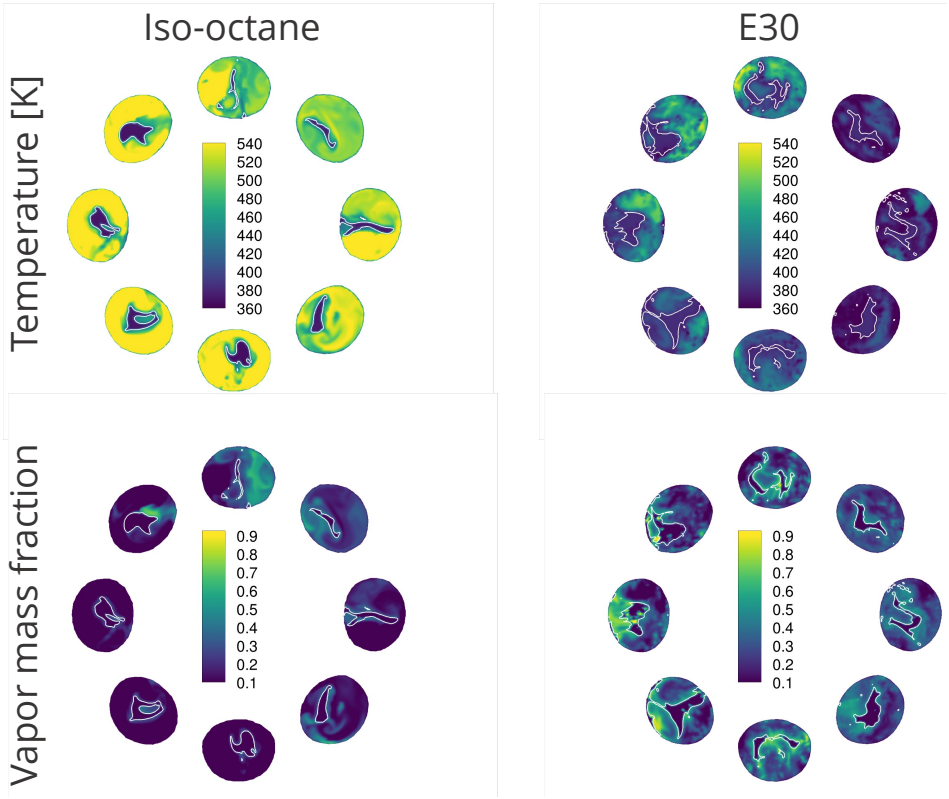

Figure 12. Flow passing through the counterbores when the injector is partially closed.